A Circuit for Simultaneous Reception of Data and Power Using a Solar Cell

Sindhubala Kadirvelu, Walter D. Leon-Salas, *Member, IEEE*, Xiaozhe Fan, Jongseok Kim, Borja Peleato, Saeed Mohammadi, and B. Vijayalakshmi

Abstract—This paper presents a circuit for simultaneous reception of optical power and data using a solar cell. The circuit employs a switched-inductor boost DC-DC converter for energy harvesting and a low-power thresholding receiver for data reception. The thresholding data receiver comprises a current-sense resistor that monitors the current output of the solar cell, an instrumentation amplifier, a band-pass filter and a comparator. A system-level analysis of an optical communication system employing the proposed circuit is presented along with a circuit-level analysis and implementation. As a proof-of-concept, the proposed circuit for simultaneous power and data reception is implemented using off-the-shelf components and tested using a custom-built test setup. Measurement results, including harvested power, electronic noise and bit error rate (BER), are reported for a GaAs solar cell and a red LED light source. Results show that 223 μW of power are harvested by the DC-DC converter at a distance of 32.5 cm and a radiated power of 9.3 mW. At a modulation depth of 50% and a transmission speed of 2.5 kbps, a BER of 1.008×10^{-3} is achieved. Measurement results reveal that the proposed solution exhibits a trade-off between harvested power, transmission speed and BER.

Index Terms—Energy harvesting, solar cells, optical communications, visible light communications.

Sindhubala Kadirvelu was with the School of Engineering Technology, Purdue University, West Lafayette, IN 47907 USA. She is now with the Electronics and Communications Engineering Department, B. S. Abdur Rahman Crescent Institute of Science and Technology, Chennai 600048, India.

Walter D. Leon-Salas and Xiaozhe Fan are with the School of Engineering Technology, Purdue University, West Lafayette, IN 47907 USA (e-mail: wleonsal@purdue.edu).

Jongseok Kim is with the CCS Graduate School of Green Transportation, Korean Advanced Institute of Science and Technology, Daejeon 34051, South Korea.

Borja Peleato is with the Department of Signal Theory and Communications, Universidad Carlos III de Madrid, 28911 Leganes, Spain.

Saeed Mohammadi is with the Electrical and Computer Engineering Department, Purdue University, West Lafayette, IN 47907 USA.

B. Vijayalakshmi is with the Electronics and Communications Engineering Department, B. S. Abdur Rahman Crescent Institute of Science and Technology, Chennai 600048, India.

Digital Object Identifier 10.1109/TGCN.2021.3087008

I. INTRODUCTION

IN THE Internet-of-Things (IoT) vision, everyday objects, such as home appliances, furniture and wearable items, seamlessly connect to the Internet to exchange information with the ultimate goal of enhancing our lives by monitoring and controlling the environment around us [1]. IoT solutions are being deployed at a very fast pace. The number of interconnected devices is expected to more than double from 9 billion in 2013 to more than 20 billion in 2020 [2]. This growth will amount to a \$1.3 trillion opportunity for health care, automotive, utilities and consumer electronics markets [1]. To be truly seamless, IoT devices must have a wireless means of communication because untethered devices can be easily integrated into everyday objects. In addition, IoT devices should be able to harvest energy from their environment to avoid frequent manual recharging or periodic battery changes. Given that radiant/luminous energy is the most ubiquitous form of energy, these two conditions can be met if light is employed to transmit data and energy [3]. Using light to transmit data and energy benefits from the growing interest in light-emitting diode (LED) based illumination [4]. Unlike other light sources, the optical power of an LED can be varied faster than the human eye can distinguish, according to an information-bearing signal. Hence, LED lighting offers an opportunity for data transmission in addition to energy-efficient illumination [5], [6].

IoT devices equipped with a solar cell would not only be able to harvest ambient radiant energy from LED lights but could also use their solar cells as photo-detectors to receive information encoded optically [7]–[18]. In an approach dubbed Optical Frequency Identification (OFID), GaAs solar cells are used as infrared light sources and employed to transmit information optically [19], [20]. Hence, a bi-directional optical communication system can be implemented using LED lights and GaAs solar cells. Such as system would be useful in indoor IoT sensing applications as shown conceptually in Fig. 1. In the downlink direction (from the LED lights to the optical wireless node), data is transmitted by the LED light and received by the solar cell. In the uplink direction (from the optical wireless node to the LED light), data is transmitted by modulating the luminescent radiation of the solar cell and received by a photo-detector next to the LED light (not shown). The LED light can be used to acknowledge a successful reception to the wireless node. When the solar cell is not being used to receive or transmit data, it harvests radiant
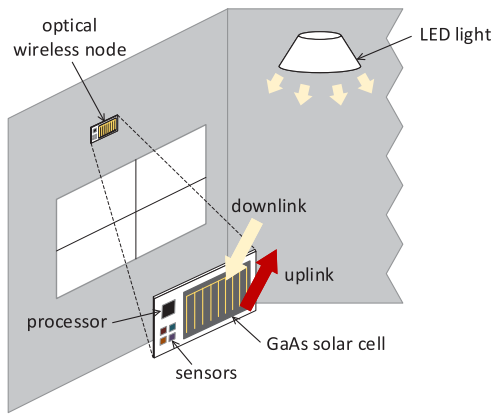
Fig. 1. Conceptual diagram of an indoor optical wireless network. A wireless communication link is established between an LED light and an optical wireless node. The wireless optical node incorporates a GaAs solar cell, which functions as a photo-detector to receive data from the LED light (downlink) and as an infrared light source to transmit data (uplink). The solar cell also harvests radiant energy from its environment resulting in a fully self-powered wireless sensor node.

energy from its environment to power itself up and/or recharge its energy reservoir. Having fully self-powered wireless nodes reduces network maintenance costs while reusing the solar cell for multiple purposes decreases fabrication costs.

Solar cell-based optical receivers for visible light communications (VLC) have been explored before in [7]–[18]. In [7], [9], [12], [13] the authors demonstrate that a solar cell can work as a photo-detector in an optical communication system but it is not shown how energy harvesting and data reception could be accomplished with the same solar cell. These solutions do not demonstrate a self-powered receiver either. In [10], [11], [14] a receiver architecture with two branches are used, one branch for data reception and the other one for energy harvesting. A capacitor is used in the data reception branch to block DC and a choke inductor is used in the energy harvesting branch to filter out the received signal. A drawback of this approach is that a farily large choke inductor is needed (10 mH), which takes occupies a relatively large space and precludes its integration on a chip or in a system-in-package (SiP) solution. Moreover, in these approaches as well as the one presented in [8], a resistor is employed to model the energy harvesting load. While a resistor provides a good first-order load approximation, it does not capture higher-order effects such as switching noise and the input capacitance of a DC-DC converter. In a more realistic implementation, the choke inductor would have to be sized such that it filters out the received signal as well as the switching noise from the DC-DC converter but because in [8], [10], [11], [14] only a resistor load is used, this case is not considered limiting its applicability. Moreover, a self-powered solution is not demonstrated. The works reported in [15], [17], [18] are self powered but achieve this condition using a solar panel, consisting of several solar cells connected in series, instead of a single solar cell. For instance, the solar panel in [17] contains 18 solar cells and has a nominal output voltage of 9 V. Hence, there is no need for a DC-DC boost converter as the solar panel generates enough voltage to directly power the receiver circuit.

However, this direct connection results in the solar panel not operating at its maximum power point. Having a DC-DC converter in between the solar cell and the receiver (load) allows for maximum power draw from the solar cell as well as voltage boosting.

In terms of modulation techniques, On-Off Keying (OOK) offers the lowest complexity in terms of hardware implementation at the transmitter and receiver sides. A downlink bit rate of 4.8 kbps was reported in [17] with OOK and a silicon solar cell. Using a signal conditioning analog circuit, the authors of [18] were able to improve the frequency response of a silicon solar cell and achieved a bit rate of 8 kbps using OOK. The work in [7] employed OOK and a pre-distortion scheme at the transmitter side and obtained a bit rate of 400 kbps at a bit error rate (BER) of 10^{-9}. Using more complex modulation techniques such as quadrature amplitude modulation (QAM) and orthogonal frequency-division multiplexing (OFDM), higher bit rates are possible [9]–[13]. For instance, a bit rate of 15.03 Mbps at a BER of 1.69×10^{-3} is reported in [9] using 16-QAM OFDM and a silicon solar cell. In [10], a bit rate of 11.84 Mbps at a BER of 1.6×10^{-3} was reported with 4-QAM OFDM and a silicon solar cell. Organic solar cells seem to have a speed advantage over silicon cells. The work in [11] reports a bit rate of 34.2 Mbps at a BER of 4.08×10^{-4} for 4-QAM OFDM using an organic PTB7:PC$_{71}$BM solar cell.

The speed advantages of QAM and OFDM over OOK come at the cost of more complex transmitter and receiver architectures. For instance, at the receiver side, the received signal undergoes the following decoding process: synchronization, matched filtering, downsampling, Fast Fourier Transform (FFT), channel estimation, equalization, and M-QAM demodulation [10]. The implementation of an OFDM receiver was reported in [9], [10] using MATLAB and a personal computer for convenience and flexibility. However, to achieve the lowest power consumption, an OFDM receiver would have to be implemented on a custom integrated circuit. An OFDM application-specific integrated circuit (ASIC) receiver fabricated in a 0.18 μm CMOS process and optimized for low power consumption was reported in [21]. The receiver consumes 32 mW of power while providing a data rate of 8 Mbps. This power consumption is still too high for a small self-powered optical wireless node. For instance, our measurements show that a 5 cm $\times$ 1.8 cm high-efficiency GaAs solar cell is able to harvest around 400 μW of power from the ambient light of a typical office with an illuminance of about 300 lux. Hence, for applications where fully self-powered wireless devices are needed, such as the one shown in Fig. 1, receiver architectures that with low power consumption are needed.

This work presents the design and validation of a circuit for simultaneous reception of power and data suitable for *self-powered* optical wireless devices. It addresses the downlink communication direction illustrated in Fig. 1. The proposed circuit is based on a low-power thresholding receiver and a switched-inductor boost DC-DC converter. It re-uses the current-sense resistor (that is normally present in solar energy harvesting systems) to pick up the received signal, which is then amplified and filtered, thus voiding the need for a
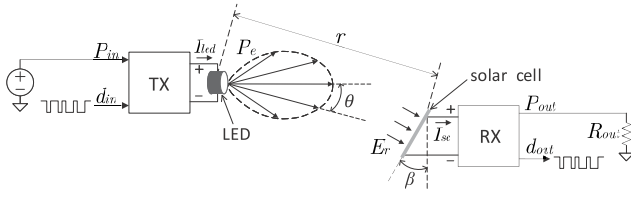
Fig. 2. System-level diagram of an optical downlink in which a solar cell is employed to receive both data and power from an LED light source.

choke inductor. Compared to previous work on solar cell-based receivers our work considers the interplay between the data receiver circuit and a DC-DC converter in terms of bandwidth, power losses and noise. The work presented here is an extension of our previous work [16] but here it is expanded with an analytical analysis and more complete experimental validation. The specific contributions of this work are: 1) system-level analysis of a solar cell-based communications link; 2) a circuit for simultaneous reception of optical power and data; 3) circuit-level analysis of the proposed solution; and 4) hardware implementation and validation of a solar cell-based communication system using discrete off-the-shelf electronic components.

The rest of this paper is organized as follows: Section II presents a system-level analysis of a solar cell-based optical communications link. Section III describes the design of the proposed circuit for simultaneous reception of data and power. Section IV presents a discrete component hardware implementation along with measurement and characterization results. Section V concludes the paper.

II. SYSTEM-LEVEL ANALYSIS

A system-level diagram of an optical communication downlink between an LED and a solar cell is shown in Fig. 2. The transmitter (TX) has a power input, P_{in}, and a data input (d_{in}). The transmitter modulates the optical power emitted by the LED (P_e) with the purpose of transmitting power and data to a solar cell positioned at a distance r and angle θ from the LED. The receiver (RX) has two outputs, a power output, P_{out}, and data output d_{out}. Due to conversion inefficiencies and the broad radiation pattern of the LED, $P_{out} < P_{in}$. Also, due to noise, errors will be introduced in d_{out}.

The radiant power received by the solar cell is given by:

$$P_r = E_r \times A_{eff} \tag{1}$$

where, E_r is the irradiance at the solar cell and A_{eff} is the effective light gathering area of the solar cell, which is equal to $A \cos(\beta)$ with A being the area of the solar cell and β the solar cell inclination angle. Also, by definition, $E_r = d\Phi/dA$, where $d\Phi$ is the radiant flux falling onto a surface element dA. Combining this result with (1) yields the following relationship:

$$P_r = \frac{d\Phi}{dA} A \cos(\beta) \tag{2}$$

The radiant intensity (or radiation pattern) of the LED is defined as the radiant flux $d\Phi$ emitted per unit solid angle $d\Omega$

in the θ direction [22]:

$$I(\theta) = \frac{d\Phi}{d\Omega} \tag{3}$$

At a distance r, and assuming a point source, the solid angle can be calculated as:

$$d\Omega = \frac{dA}{r^2} \tag{4}$$

Combining (3) and (4) yields:

$$I(\theta) = \frac{d\Phi}{dA} r^2 \tag{5}$$

A common radiation pattern used when modelling LEDs is the Lambertian radiation pattern. The Lambertian radiation pattern of mode number *m* having uniaxial symmetry is given by [23]:

$$I(\theta) = \frac{m+1}{2\pi} \cos^m(\theta) P_e \tag{6}$$

where, $m = -\ln(2)/\ln(\cos(\alpha_{1/2}))$, $\alpha_{1/2}$ is the half-power semi-angle [24] and P_e is the total radiant flux (power) emitted by the LED. Combining (2), (5) and (6) results in the following expression for the optical power received by the solar cell:

$$P_r = \frac{m+1}{2\pi r^2} \cos^m(\theta) \cos(\beta) \cdot A \cdot P_e \tag{7}$$

We define the gain of the optical path G_{op} as:

$$G_{op} = \frac{P_r}{P_e} = \frac{m+1}{2\pi r^2} \cos^m(\theta) \cos(\beta) \cdot A \tag{8}$$

At the solar cell, absorbed photons generate electron-hole pairs which contribute to the photo-generated current I_{ph} of the solar cell. The photo-generated current is proportional to the received optical power via the responsivity R_λ as follows:

$$I_{ph} = R_\lambda P_r. \tag{9}$$

Combining (8) and (9) results in:

$$I_{ph} = R_\lambda \cdot G_{op} \cdot P_e. \tag{10}$$

Equation (10) shows that I_{ph} is directly proportional to the power emitted by the LED P_e. Hence, any modulation applied by the transmitter on P_e can be detected by measuring I_{ph}. Furthermore, this analysis provides an expression for the gain of the optical path (G_{op}), a useful parameter when measuring the end-to-end gain and frequency response of the communication system.

To illustrate how the photo-current I_{ph} can be measured, let us consider the equivalent circuit of a solar cell shown in Fig. 3. In the figure, the solar cell is loaded with a load ($C_{load} \| R_{load}$). This load is representative of a DC-DC converter that will be used later on to boost and regulate the solar cell's output voltage. The diode in the equivalent circuits models the "knee" in the current-vs-voltage ($I - V$) curve and it is modelled with the Shockley diode equation: $I_d = I_s(e^{V_d/nV_T} - 1)$, where I_s is the reverse saturation current, n is the diode ideality factor and V_T is the thermal voltage. The resistance R_{sh} is a shunt resistance that models the load presented to the current harvested near the edges of the solar cell, R_{sr} is the solar cell's series resistance due
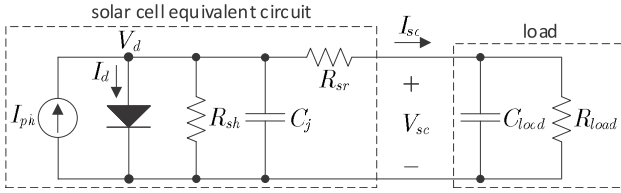
Fig. 3. Equivalent circuit of a solar cell loaded with a resistor (R_{load}) and a capacitor (C_{load}) in parallel.
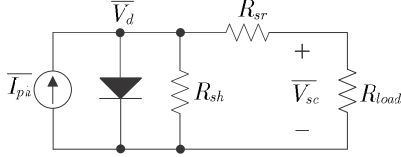

Fig. 4. Equivalent DC circuit of loaded solar cell.

to contacts and connections and C_j is the solar cell's junction capacitance [25]. Although these parameters change with frequency, here, they are assumed to be frequency independent because of the relatively narrow frequency range of operation of the proposed receiver. To simplify our analysis we will assume that $R_{sr} \approx 0$. This assumption results in an error of less than 0.01 dB in the estimation of the pass-band gain of the receiver and less than 0.05% in the estimation of the energy harvesting efficiency.

Our circuit analysis will first establish the DC operating point and then it will proceed to linearize the diode around the DC operating point in order to perform a small-signal AC analysis. In this analysis, every voltage and current will be assumed to have a DC component (denoted with a bar over the variable name) and an AC component (denoted with lower case letters). For instance, I_{ph} will be written as $I_{ph} = \overline{I_{ph}} + i_{ph}$, where $\overline{I_{ph}}$ is the DC component and i_{ph} is the AC component.

A. DC Analysis

Opening C_j and C_{load} for DC analysis yields the equivalent circuit show in Fig. 4. Solving this circuit for $\overline{V_{sc}}$ yields the following result:

$$\overline{V_{sc}} = \frac{k_3 - W(a_1)}{k_2} \tag{11}$$

where,

$$k_1 = \frac{1}{nV_T}$$
$$k_2 = \frac{1}{I_s R_{eq}}$$
$$k_3 = \frac{\overline{I_{ph}} + I_s}{I_s}$$
$$a_1 = \frac{k_1}{k_2} e^{k_1 k_3 / k_2} \tag{12}$$

$R_{eq} = R_{load} \| R_{sh}$ and $W(\cdot)$ is the Lambert-W function. The Lambert-W function provides an explicit solution to an equation of the form: $xe^x = z$ as $x = W(z)$ [26]. From the circuit in Fig. 4, $\overline{I_{sc}} = \overline{V_{sc}}/R_{load}$. The DC power delivered to the
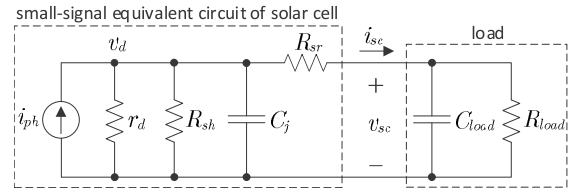
load is $P_{load} = \overline{V_{sc}} \times \overline{I_{sc}}$ and is maximum at the maximum power point (MPP). The output resistance of the solar cell at the MPP is $R_{mpp} = V_{mpp}/I_{mpp}$. This DC analysis is needed to obtain a value for the operating point of the solar cell ($\overline{V_{sc}}, \overline{I_{sc}}$), which will be used to perform an AC analysis to determine the frequency response and the bandwidth of the solar cell.

B. AC Analysis

The AC analysis presented here will provide the insight needed to select between a current-sense and a voltage-sense receiver architectures. The current-sense architecture uses the current generated by the solar cell as its input while the voltage-sense architecture uses the voltage across the solar cell as its input. Fig. 5 shows the small-signal equivalent circuit of a loaded solar cell. The diode has been replaced by small-signal resistor r_d. An expression for r_d was calculated by applying the Taylor series to the Shockley diode equation and then calculating the slope $\partial I_d / \partial V_d$ at $\overline{V_{sc}}$. The resulting expression for r_d is as follows:

$$r_d = \frac{nV_T}{I_s} e^{-\overline{V_{sc}}/nV_T} \tag{13}$$

Solving the small-signal equivalent circuit in Fig. 5 yields the following expressions for i_{sc} and v_{sc}:

$$i_{sc} = i_{ph} \frac{Z_d}{Z_d + Z_{load}}$$
$$v_{sc} = Z_{load} \cdot i_{sc} \tag{14}$$

where, $Z_d = r_d \| R_{sh} \| 1/sC_j$, $Z_{load} = R_{load} \| 1/sC_{load}$ and $s = j2\pi f$ (with f being frequency in Hz). Using (14), the transfer functions i_{sc}/i_{ph} and v_{sc}/i_{ph} can be computed. Fig. 6 shows a plot of the magnitude of these two transfer functions for $\overline{I_{ph}} = 508$ μA, $R_{sh} = 138.8$ kΩ, $C_j = 798$ nF, $R_{load} = R_{mpp} = 1.36$ kΩ and $C_{load} = 10$ μF. The values of $\overline{I_{ph}}$ and R_{sh} were estimated from a measured current-vs-voltage (IV) curve of a 5 cm × 1.8 cm GaAs solar cell from Alta Devices under typical office illumination (around 400 lux). The value of capacitance C_j was estimated using the time-domain technique described in [27]. Notably, the v_{sc}/i_{ph} transfer function has a relatively large DC trans-impedance gain of 56 dΩ, however, it has a corner frequency of only 40 Hz and exhibits a low-pass response. To efficiently utilize this type of response, advanced encoding techniques such as bit loading would be required [11] but at the expense of increasing the complexity and power consumption of the receiver. On the other hand, the i_{sc}/i_{ph} transfer function exhibits a pass-band with a wider frequency range ($\sim$ 700 kHz) but lower gain (-0.6 dB). Due to the wide pass-band feature of the i_{sc}/i_{ph}
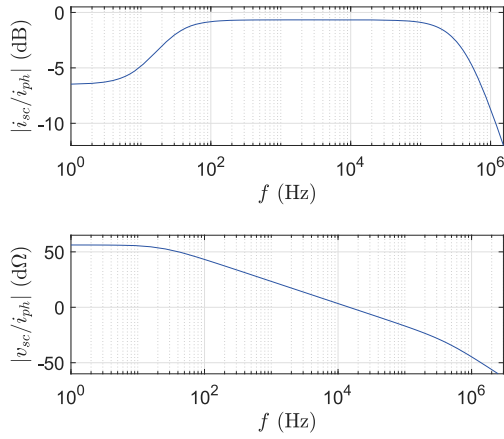
Fig. 6. Magnitude plots of transfer functions i_{sc}/i_{ph} (top) and v_{sc}/i_{ph} (bottom).
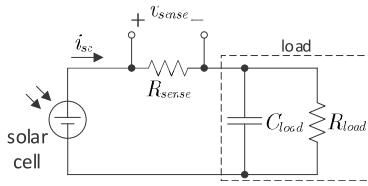

Fig. 7. Schematic diagram of circuit employed to measure output current of a solar cell. The small-signal voltage v_{sense} across the current-sense resistor R_{sense} is proportional to the small-signal current i_{sc}.

Fig. 8. Magnitude of transfer function $H_{sense} = v_{sense}/i_{ph}$ for different values of current-sense resistor R_{sense}.

Fig. 9. Energy harvesting efficiency $\eta = P_{load}/P_{mpp} \times 100 \%$ for different values of current-sense resistor R_{sense}.

transfer function, in this work, the output current of the solar cell i_{sc} will be used to estimate the photo-generated current i_{ph} (current-sense architecture).

To measure the output current of the solar cell, a current-sense resistor (R_{sense}) is added in series with the solar cell as shown in Fig. 7. The small-signal voltage v_{sense} developed across this resistance is proportional to the small-signal output current of the solar cell i_{sc}.

Using the small-signal equivalent circuit of the solar cell shown in Fig. 5, the following expression for the transfer function $H_{sense} = v_{sense}/i_{ph}$ can be derived:

$$H_{sense} = \frac{Z_d R_{sense}}{Z_d + R_{sr} + R_{sense} + Z_{load}} \qquad (15)$$

The magnitude of this transfer function is plotted in Fig. 8 for different values of R_{sense}. Notably, as the value of R_{sense} increases, the pass-band gain of H_{sense} also increases but at the cost of reduced bandwidth. Thus, small values of R_{sense} are preferred to keep a wide bandwidth. To boost the pass-band gain, an amplifier will have to be used.

Another motivation for using small values for R_{sense} comes from the power dissipated across this resistance. Increasing R_{sense} increases the power dissipated across it and lowers the power delivered to the load. Fig. 9 shows the energy harvesting efficiency defined as $\eta = P_{load}/P_{mpp} \times 100 \%$, where P_{load} is the power delivered to the load. This figure shows that to maximize the power delivered to the load, small values of R_{sense} should be used.
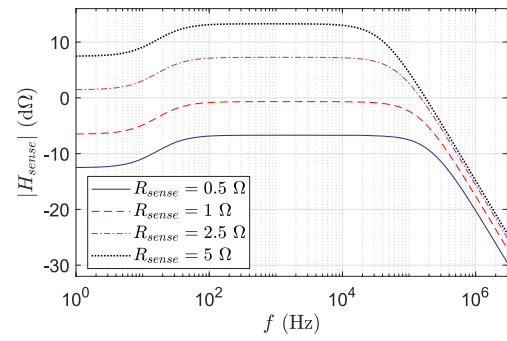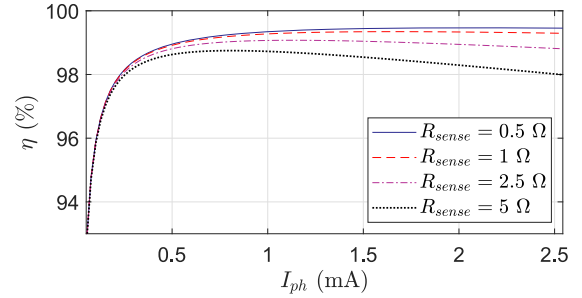
Our hardware implementation employs a 1 Ω resistor for R_{sense} because it results in a small drop in energy harvesting efficiency ($\sim$0.3%) while maintaining a wide bandwidth. Current-sense resistors are commonly employed in solar energy harvesting systems to monitor the solar cell's output current and adjust the operation of a DC-DC converter in order to maximize the power drawn from the solar cell. Reusing the current-sense resistor for data reception purposes would lead to savings in circuit complexity.

III. CIRCUIT-LEVEL DESIGN

The main constraint in the design of a circuit for the envisioned application is the amount of harvestable ambient power. Fig. 10 shows the measured IV curve of a 5 cm $\times$ 1.8 cm GaAs solar cell in an office setting with an illumination of around 400 lux. The maximum power delivered by this solar cell under these conditions is 347 μW. Hence, any data receiver and energy harvesting circuit will have to consume less than this amount to enable continuous self-powered operation. Furthermore, the solar cell's output voltage at the MPP is 0.74 V. This voltage will have to be stepped up to a higher level in order to power other electronic circuits and/or charge a battery.

Fig. 11 shows a diagram of the proposed circuit for simultaneous reception of power (energy harvesting) and data using a solar cell as the transducer. The proposed circuit consists of a solar cell, a current-sense resistor, a boost DC-DC converter and a data receiver. The function of the boost DC-DC converter is to draw power from the solar cell while boosting the relatively low output voltage of a solar cell (between 0.6 to 1.0 V depending on illumination conditions) to a higher
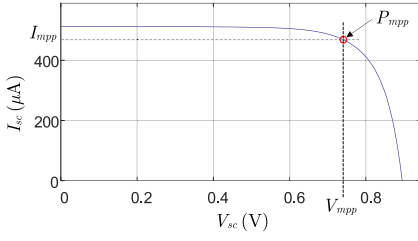
Fig. 10. Measured IV curve of a GaAs solar cell in an indoor office environment. The MPP is marked with a circle.
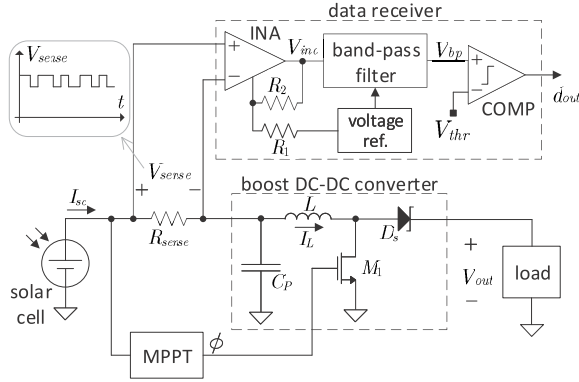

Fig. 11. Schematic diagram of proposed circuit for simultaneous reception of power and data using a solar cell.

voltage that is compatible with most electronic loads. This converter uses inductor L and MOSFET switch M_1 to transfer charge from the solar cell to the load. It works in two phases. In Phase I, when the clock signal ϕ is high, M_1 closes and the inductor gets charged by the solar cell and capacitor C_P. In Phase II, when ϕ is low, M_1 opens and the inductor discharges into the load while the solar cell charges capacitor C_P. The Schottky diode D_s prevents charges from moving from capacitor C_L to the inductor. The input impedance of this DC-DC converter is a function of the duty cycle of the clock signal ϕ. At a certain duty cycle value, the input impedance matches the output impedance of the solar cell resulting in maximum power drawn from the solar cell. Adjusting the clock's duty cycle is the function of an MPP tracker (MPPT). The load connected to the DC-DC converter includes a voltage regulation and possibly a battery charging stages.

The data receiver consists of an instrumentation amplifier (INA), a band-pass filter and a comparator (COMP). The INA amplifies the voltage across R_{sense} and, due to its high input impedance, it isolates the solar cell and the DC-DC converter from the rest of receiver circuitry. The INA's gain is set by resistors R_1 and R_2. The band-pass filter filters out DC and low frequency noise (60 Hz) and high frequency noise due to the switching action of the DC-DC converter and high-frequency ambient noise from fluorescent lamps. Finally, the comparator generates a fully digital signal.

A hardware implementation using discrete off-the-shelf components for rapid prototyping is considered here. Although our results will be specific to the implemented circuit, the overall design methodology is still applicable to integrated

solutions. Our design must consider the interplay of several factors, some of which have conflicting requirements. For instance, to maximize the capacity of the data receiver, its bandwidth should be maximized and its noise floor should be minimized. However, maximizing the bandwidth and minimizing noise requires higher power consumption. In addition, to minimize the effects of the switching noise from the DC-DC converter into the data receiver, we could lower the upper cutoff frequency of the band-pass filter or increase the switching frequency. If the upper cutoff frequency is reduced, the bandwidth and therefore the capacity of the receiver will be reduced. On the other hand, if the switching frequency is increased, the efficiency of the DC-DC converter will decrease due to parasitic capacitances of the switch.

This rich design space will be approached using the following heuristic approach: 1) set power budget, receiver gain and the switching frequency of the DC-DC converter; 2) select the upper cutoff frequency of the band-pass filter to achieve at least A_{tt} dB of attenuation of the switching noise; 3) find a set of amplifiers that can deliver the desired gain and bandwidth; 4) estimate power consumption; and 5) if power consumption exceeds the power budget, reduce the receiver gain or relax A_{tt} and repeat the process.

To get a sense of how much gain is needed in the data receiver, consider the scenario depicted in Fig. 1 with an LED light with a radiated power of 5 W and a half-power semi-angle of 30°. Using (10), the photo-current generated in a 5 cm × 1.8 cm GaAs solar cell at a distance of 2 m is 476 μA. Approximating the solar cell's output current at the MPP as $I_{mpp} = 0.85 \times I_{ph}$ and considering a minimum modulation depth of 10%, a receiver gain (including the gain of the INA and the band-pass filter) of 60 dB will yield an overdrive voltage at the comparator's input of $\sim$20 mV, which is sufficient to trigger a low-power comparator.

Let us set the power budget for the data receiver to 174 μW or 50% of the maximum power generated by a 5 cm × 1.8 cm GaAs solar cell under the illumination of a typical office (400 lux). The receiver gain is set to 60 dB and the switching frequency of the DC-DC converter to 100 kHz. Using a second-order band-pass filter and an upper cutoff frequency of 10 kHz yields a 40 dB attenuation for the switching noise. The low-power INA322 instrumentation amplifier [28] and the TLV2379 operational amplifier [29] have just enough gain-bandwidth product to deliver a combined gain of 60 dB (40 dB from the instrumentation amplifier and 10 dB for each stage of the second-order band-pass filter) up to a frequency of 10 kHz. At a 3.0 V supply voltage, the INA322 consumes 120 μW and the TLV2379 consumes 24 μW, resulting in a total power consumption for the data receiver of 174 μW (including the power consumption of the voltage reference and the low-power comparator TLV7011 [30]). A fractional open circuit MPPT requires three opamps (including the oscillator) [32] and if it is implemented using low-power discrete components, a power consumption of 40 μW can be achieved. Integrated MPPT solutions can achieve even lower power consumption [33]–[35]. Therefore, the proposed

receiver can be *fully powered* by energy harvested from indoor ambient light.

Noise is another limiting factor of the data receiver and it negatively impacts its performance. Internal noise sources, such as electronic device noise and switching noise, are inherent to the circuit operation and, although they are unavoidable, their impact can be minimized. External or ambient noise depends on the receiver's surroundings and can range from low-frequency noise from sunlight or incandescent bulbs to high-frequency from fluorescent or LED lights. In this work a band-pass active filter is employed to remove low and high-frequency noise is employed.

IV. HARDWARE IMPLEMENTATION AND RESULTS

This section reports the results of several measurements aimed at characterizing different aspects, such as frequency response, energy harvesting and bit error rate (BER), of the proposed power and data receiver circuit. To this end, the test setup shown in Fig. 12 was built. The test setup consists of an LED driver, a GaAs solar cell from Alta Devices, the power and data receiver circuit, and electronic test equipment such as oscilloscope, power supply and waveform generators. The test setup was placed inside a light enclosure to block ambient noise during frequency response measurements. For all other measurements this box was kept open. The receiver circuit was placed inside an aluminum box to reduce electro-magnetic interference.

The LED driver consists of a voltage-to-current converter, which sets the current through the LED, I_{led}, proportional to the modulating input V_{mod} as follows:

$$I_{led} = \frac{V_{mod}}{R_E}. \tag{16}$$

For the results reported here, the DC component of the modulating input is set to $\overline{V_{mod}} = 120$ mV resulting in a radiated power of 9.3 mW. At a distance $r = 32.5$ cm, a maximum power of 340 μW is generated by the solar cell, which is equivalent to the power generated in an office setting with an illumination of around 400 lux. The amplifiers in the receiver circuit are powered by a Li-ion battery and a low-power voltage regulator that regulates the battery output voltage to 3.0 V. The LED is a high-power red LED (LXM5-PD01 LUXEON Rebel) outfitted with a Fraen 9° lens with 85% transmittance. The radiant flux emitted by the LED is proportional to its current [36]. Hence, we can write:
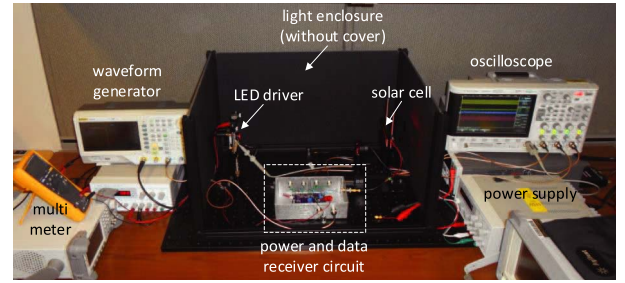
$$P_e = T_{lens} \cdot G_{led} \cdot I_{led} \tag{17}$$

where, P_e is the radiant flux emitted by the LED assembly, T_{lens} is the transmittance of the LED lens and G_{led} is a factor that relates the LED current with its optical power and has a value of 0.88 W/A for the chosen LED [36].
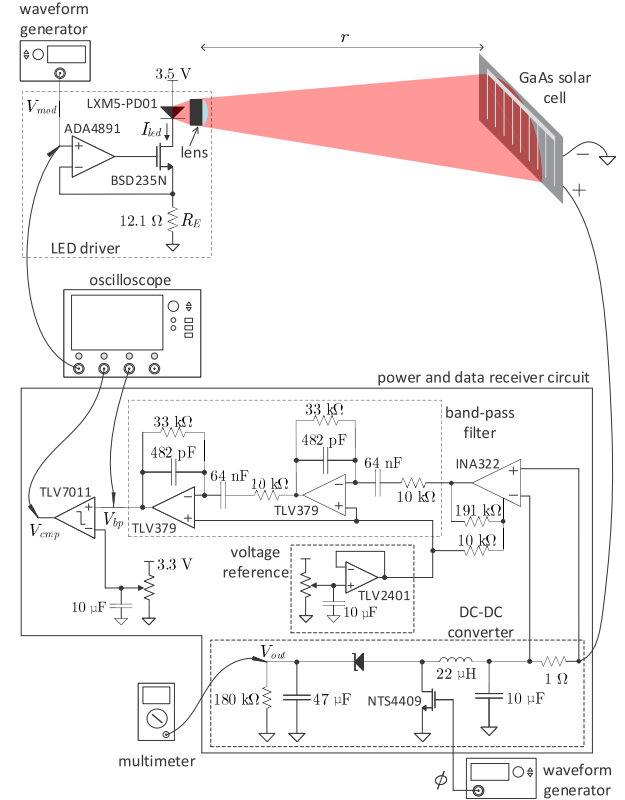
Combining (16), (17) and (10) yields:

$$I_{ph} = \underbrace{\left(\frac{R_\lambda \cdot G_{op} \cdot T_{lens} \cdot G_{led}}{R_E} \right)}_{G_0} V_{mod}. \tag{18}$$

Equation (18) shows that the photo-generated current I_{ph} is directly proportional to the modulating input V_{mod}. This

(a)

(b)

Fig. 12. Test setup. (a) photograph; (b) schematic diagram.

linear relationship allows us to measure the frequency response of the entire optical communication system. The frequency response of the communication system can also be analytically modelled as follows:

$$\frac{v_{bp}}{v_{mod}} = G_0 \cdot H_{sense} \cdot H_{ina} \cdot H_{bp} \tag{19}$$

where, H_{ina} and H_{bp} are the frequency responses of the INA and the band-pass filter, respectively. Expressions for these frequency responses are derived in Appendices A and B.

Fig. 13 shows the modelled and the measured frequency responses of the optical communication system for $r = 32.5$ cm, $\theta = 0°$, $\beta = 0°$, $R_\lambda = 0.457$ A/W, $\alpha_{1/2} = 9°$ and $A = 5$ cm $\times$ 1.8 cm. The frequency response was measured by applying a frequency sweep to the input V_{mod}
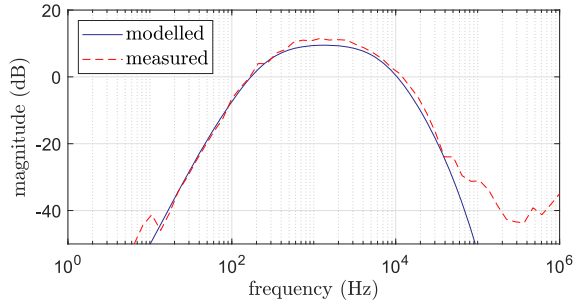
Fig. 13. Modelled and measured frequency response of the optical communication system.
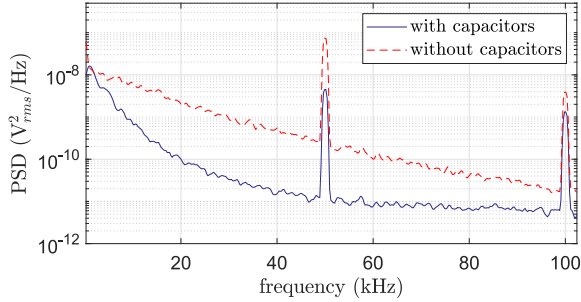

Fig. 15. Measured output voltage of DC-DC converter as a function of the clock's frequency and duty cycle ρ.

Fig. 14. Measured PSD at the output of the band-pass filter (AC coupled). The PSD was measured with the Agilent 35670A signal analyzer.

Fig. 16. Measured waveforms when the LED optical output power is modulated with a pseudo-random bit sequence encoded with a Manchester code. V_{mod} is the modulating input, V_{bp} is the output of the band-pass filter (AC coupled) and V_{cmp} is the output of the comparator.

of the LED driver and observing the output of the band-pass filter V_{bp}. Notably, the modelled and the measured frequency responses agree fairly well demonstrating the validity of the derived analytical model. To assess the effectiveness of the band-pass filter at removing switching and ambient noise, the power spectral density (PSD) at the output of the filter was measured. For comparison, the PSD was measured with and without the capacitors in the filter. The measured PSDs for $f_{sw} = 50$ kHz and for constant illumination are shown in Fig. 14. From the measured PSDs, the root mean square (RMS) values of the noise at the output of the filter were calculated to be 7.769 mV$_{rms}$ (with the filter's capacitors) and 15.892 mV$_{rms}$ (without the filter's capacitors). Hence, the filter is effective at removing switching and ambient noise.

To characterize the energy harvesting performance of the proposed circuit, the output voltage of the DC-DC converter V_{out} was measured while the duty cycle (ρ) of the clock signal ϕ was varied. This procedure was repeated for different frequencies of the clock signal. Fig. 15 shows the results of this characterization. As it can be seen from the figure, lowering the clock's frequency results in a higher output voltage and hence a higher power delivered to the load. The conversion efficiency of the DC-DC converter, defined as the maximum power delivered to the load over the maximum power generated by the solar cell, is 67% for $f_{sw} = 50$ kHz, 56.4% for $f_{sw} = 100$ kHz and 42% for $f_{sw} = 200$ kHz. The conversion efficiency decreases as the clock frequency increases due to frequency-dependent losses in the MOSFET switch. The efficiency of the DC-DC converter can be further improved by using an active diode [37] instead of the Schottky diode and decreasing the size of the current-sense resistor.
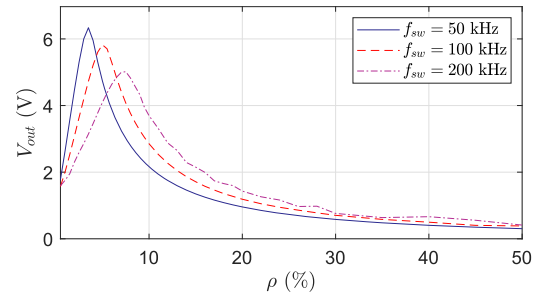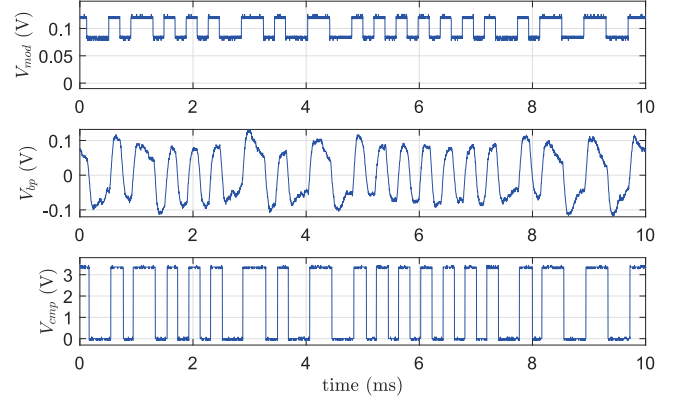
Finally, a measurement to characterize the BER of an optical communication system using the proposed solar cell-based receiver was carried out. For this experiment, a 20-tap linear feedback register was employed to generate a long pseudo-random bit sequence. Each bit of this sequence was Manchester encoded such that a logic 1 bit was encoded with a low-to-high transition and a logic 0 bit was encoded with a high-to-low transition. This ensures periodical transitions in the signal, preventing the receiver from miss-identifying a long string of identical bits with a DC offset. The resulting waveform was scaled to match the input range of the LED driver and loaded to the waveform generator whose output is connected to the modulating input, V_{mod}, of the LED driver. At the receiver end, the output of the band-pass filter, V_{bp}, and the output of the comparator, V_{cmp}, were recorded with an oscilloscope. Fig. 16 shows a portion of these waveforms.

The recorded V_{mod} and V_{cmp} waveforms were compared using a personal computer to determine the BER. The BER was measured for 10^6 transmitted bits and for different values of the clock frequency f_{sw}, the bit duration T_{bit} and the modulation depth m. The modulation depth is defined here as the ratio between the amplitude of the transmitted bits and the modulating input when no bits are transmitted ($\overline{V_{mod}}$). For instance, the bit amplitude of the transmitted waveform in Fig. 16 is 40 mV, thus, it has a modulation depth of 33%. Fig. 17 shows the measured BER for $T_{bit} = 100$ μs (17(a)) and for $T_{bit} = 400$ μs (17(b)). Notably, the BER is reduced
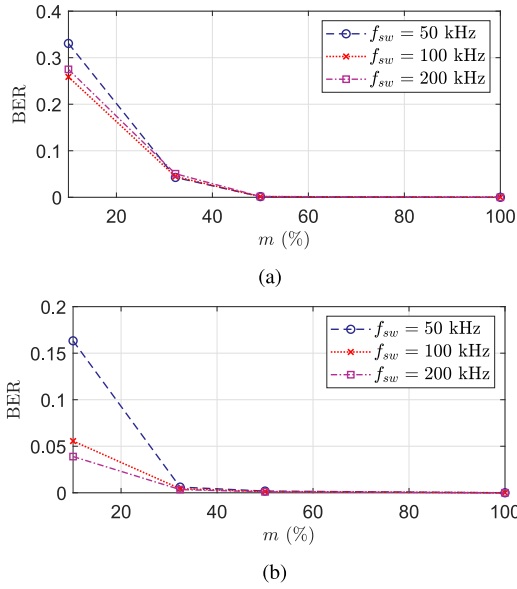
(a)

(b)

Fig. 17. Measured BER for different values of modulation depth and switching frequency. (a) $T_{bit} = 100$ μs; (b) $T_{bit} = 400$ μs.
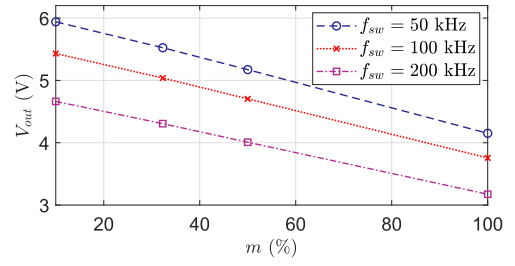

Fig. 18. Measured output voltage of the DC-DC converter as a function of the modulation depth and the clock frequency.

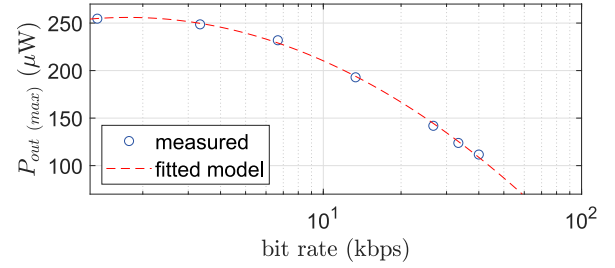Fig. 19. Illustration of trade-off between the maximum harvested power and transmission speed (bit rate).

as f_{sw} increases due to the switching noise filtering action of the band-pass filter. For instance, for $T_{bit} = 100$ μs (equivalent to a transmission speed of 10 kbps), $f_{sw} = 200$ kHz and $m = 33\%$, a BER of 5.066×10^{-2} is achieved. If T_{bit} is increased to 400 μs (equivalent to a transmission speed of 2.5 kbps), this BER decreases to 3.445×10^{-3}, which is within the reach of error-correcting codes [38]. On the other hand, if m is increased to 50%, the BER falls to 1.008×10^{-3}. This result shows that to improve the BER, the transmission speed should be reduced (T_{bit} increased) or the modulation depth should be increased.

As the modulation depth is increased, the average optical power transmitted to the solar cell and the average power delivered to the load decreases. The measured average output voltage of the DC-DC converter for different clock frequencies is shown in Fig. 18. This result highlights another trade-off in the proposed power and data receiver circuit, namely, BER performance is traded with how much power is delivered to the load. If the target application cannot tolerate a decrease in harvested power, the BER can still be improved by decreasing the transmission speed (increasing T_{bit}). It is worth noting that the speed performance of the proposed receiver is fundamentally limited by the low-power constraint imposed by the target environment, a typical office of home scenario where only a few hundred μW can be harvested. Due to their low-power consumption, the amplifiers employed also have low gain-bandwidth products and are not able to amplify fast-changing signals.

To increase the transmission speed, the bandwidth of the band-pass filter has to be increased. For Manchester coding, the upper cut-off frequency of the filter, f_H, should be selected as $1.5 \times$ (bit rate) [39]. Furthermore, to achieve sufficient attenuation of the switching noise: $f_H = f_{sw}/5$. Hence, bit rate = $f_{sw}/7.5$. On the other hand, as f_{sw} increases, the maximum output voltage of the DC-DC converter, V_{out} (and

consequently its output power $P_{out} = V_{out}^2/R_{load}$) decreases (see Fig. 15). The trade-off between the maximum harvested power, $P_{out\ (max)}$, and transmission speed is illustrated in Fig. 19, where $P_{out\ (max)}$ was measured for f_{sw} ranging from 10 kHz to 300 kHz.

The figure also shows the following fitted model:

$$P_{out\ (max)} = p_1(\log_{10}(\text{bit rate}))^2 + p_2 \log_{10}(\text{bit rate}) + p_3 \quad (20)$$

where, $p_1 = -7.972 \times 10^{-5}$, $p_2 = 5.171 \times 10^{-4}$ and $p_3 = -5.826 \times 10^{-4}$. This model shows that decreasing the bit rate below 3 kpbs does not result in a significant improvement of the maximum harvested power. It should be noted that in order to increase the bit rate above approximately 13 kbps, opamps with larger gain-bandwidth products and consequently higher power consumption, such as the TLV9042, will be needed to implement the band-pass filter. This opamp change would increase the power consumption of the receiver by approximately 36 μW.

V. CONCLUSION

A circuit solution for simultaneous reception of optical power and data using a solar cell has been presented. This solution employs a switched-inductor boost DC-DC converter for power harvesting and a thresholding receiver for data reception. It was shown that if a solar cell is loaded with a DC-DC converter, the cell's output current has a wider frequency response than its voltage. Hence, in the proposed received a current-sense resistor was used to monitor the output current of the solar cell. A system-level analysis of an optical communication system employing the solar cell receiver was also presented along with a circuit-level design methodology and analysis. A prototype of the proposed solution was built using
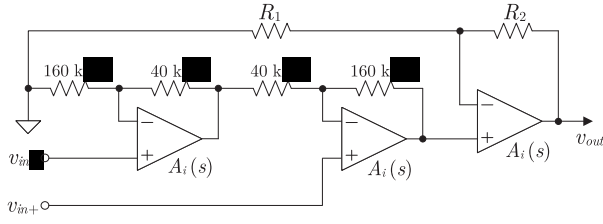
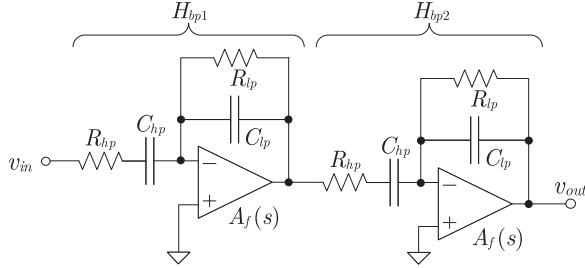Fig. 20. Small-signal equivalent circuit of instrumentation amplifier.

Fig. 21. Small-signal equivalent circuit of the second-order active band-pass filter.

off-the-shelf discrete components for rapid prototyping. The prototype employed a GaAs solar cell and an LED light source and was used to assess the performance of the proposed power and data receiver circuit. Performance was assessed for harvested power, electronic noise and BER. Measurement results revealed that the proposed solution exhibits a trade-off between harvested power, transmission speed and BER. For instance, to optimize harvested power, low clock frequencies and low modulation depths must be employed. However, low clock frequencies and low modulation depths result in low signal-to-noise ratios and therefore in increased BER. Ultimately, it is the target application that will dictate which performance aspects should be maximized.

APPENDIX A
INSTRUMENTATION AMPLIFIER

The INA322 is a three-opamp instrumentation amplifier as shown in Fig. 20 [28].

From this circuit, the following transfer function $H_{ina} = v_{out}/(v_{in+} - v_{in-})$ can be derived:

$$H_{ina} = \left(\frac{5A_i(s)(8A_i(s)+5)}{2(5+4A_i(s))(5+A_i(s))} \right) \frac{(R_1+R_2)A_i(s)}{R_1+R_2+R_1A_i(s)} \tag{21}$$

where, $A_i(s)$ is the transfer function of the internal opamps. For the INA322, these opamps are estimated to have a DC gain and a gain-bandwidth product of 100 dB and 700 kHz, respectively.

APPENDIX B
BAND-PASS FILTER

The filter employed in this work is an active continuous-time second-order filter as shown in Fig. 21.

The transfer function of this filter is $H_{bp} = H_{bp1} \times H_{bp2}$, where H_{bp1} and H_{bp2} are the transfer functions of each filter

stage and are given by:

$$H_{bp1} = H_{bp2}$$
$$= \frac{-A_f(s)\big(R_{lp}\|1/sC_{lp}\big)}{\big(1+A_f(s)\big)\big(R_{hp}+1/sC_{hp}\big)+R_{lp}\|1/sC_{lp}} \tag{22}$$

Here, $A_f(s)$ is the transfer function of the opamps employed to build the band-pass filter. For the TLV379 opamp, the DC gain is 120 dB and the gain-bandwidth product is 100 kHz [29].

REFERENCES

[1] J. Gubbi, R. Buyya, S. Marusic, and M. Palaniswami, "Internet of Things (IoT): A vision, architectural elements and future directions," *Future Gener. Comput. Syst.*, vol. 29, no. 7, pp. 1645–1660, 2013.

[2] C. MacGillivray *et al.* *Worldwide Internet of Things Forecast.* Accessed: Apr. 16, 2019. [Online]. Available: https://www.idc.com/getdoc.jsp?containerId=US44281718

[3] C.-W. Chen, "Visible light communications for the implementation of Internet-of-Things," *Opt. Eng. Lett.*, vol. 55, no. 6, pp. 1–3, 2016.

[4] A. Jovicic and J. Li, "Visible light communication: Opportunities, challenges and path to market," *IEEE Commun. Mag.*, vol. 51, no. 12, pp. 26–32, Dec. 2013.

[5] H. Elgala, R. Mesleh, and H. Haas, "Indoor optical wireless communication: Potential and state-of-the-art," *IEEE Commun. Mag.*, vol. 49, no. 9, pp. 56–62, Sep. 2011.

[6] H. Haas, L. Yin, Y. Wang, and C. Chen, "What is LiFi?" *J. Lightw. Technol.*, vol. 34, no. 6, pp. 1533–1544, Mar. 15, 2016.

[7] H.-Y. Chen, K. Liang, C.-Y. Chen, S.-H. Chen, C.-W. Chow, and C.-H. Yeh, "Passive optical receiver for visible light communication (VLC)," in *Proc. IEEE Region 10 Conf. TENCON*, Nov. 2015, pp. 1–2.

[8] J. Fakidis, M. Ijaz, S. Kucera, H. Claussen, and H. Haas, "On the design of an optical wireless link for small cell backhaul communication and energy harvesting," in *Proc. IEEE Annu. Int. Symp. Pers. Indoor Mobile Radio Commun. (PIMRC)*, Sep. 2014, pp. 58–62.

[9] R. Sarwar *et al.*, "Visible light communication using a solar-panel receiver," in *Proc. IEEE Int. Conf. Opt. Commun. Netw. (ICOCN)*, Aug. 2017, pp. 1848–1853.

[10] Z. Wang, D. Tsonev, S. Videv, and H. Haas, "On the design of a solar-panel receiver for optical wireless communications with simultaneous energy harvesting," *IEEE J. Sel. Areas Commun.*, vol. 33, no. 8, pp. 1612–1623, Aug. 2015.

[11] S. Zhang *et al.*, "Organic solar cells as high-speed data detectors for visible light communications," *Optica*, vol. 2, no. 7, pp. 607–610, 2015.

[12] Z. Wang, D. Tsonev, S. Videv, and H. Haas, "Towards self-powered solar panel receiver for optical wireless communications," in *Proc. IEEE Int. Conf. Commun. (ICC)*, Jun. 2014, pp. 3348–3353.

[13] E. Bialic, L. Maret, and D. Kténas, "Specific innovative semi-transparent solar cell for indoor and outdoor LiFi applications," *Appl. Opt.*, vol. 54, no. 27, pp. 8062–8069, 2015.

[14] Y. Wang *et al.*, "Spectrum effect on output characteristics of wireless energy and data hybrid transmission system using a solar panel," in *Proc. Int. Conf. Inf. Opt. Photon. (CIOP)*, 2018, Art. no. 1096455.

[15] J. Li, A. Lu, G. Shen, L. Li, C. Sun, and F. Zhao, "Retro-VLC: Enabling battery-free duplex visible light communication for mobile and IoT applications," in *Proc. Int. Workshop Mobile Comput. Syst. Appl. (HotMobile)*, Feb. 2015, pp. 21–26.

[16] X. Fan and W. D. Leon-Salas, "A circuit for simultaneous optical data reception and energy harvesting," in *Proc. IEEE Int. Midwest Symp. Circuits Syst.*, 2017, pp. 831–834.

[17] S.-H. Lee, "A passive transponder for visible light identification using a solar cell," *IEEE Sensors J.*, vol. 15, no. 10, pp. 5398–5403, Oct. 2015.

[18] B. Malik and X. Zhang, "Solar panel receiver system implementation for visible light communication," in *Proc. IEEE Int. Conf. Electron. Circuits Syst. (ICECS)*, Dec. 2015, pp. 502–503.

[19] W. D. Leon-Salas and X. Fan, "Solar cell luminescence modulation for optical frequency identification," *IEEE Trans. Circuits Syst.*, vol. 66, no. 5, pp. 1981–1992, May 2019.

[20] W. D. Leon-Salas and X. Fan, "Exploiting luminescence emissions of solar cells for optical frequency identification (OFID)," in *Proc. IEEE Int. Symp. Circuits Syst. (ISCAS)*, May 2018, pp. 1–5.

[21] H. Zou and B. Daneshrad, "VLSI implementation for a low power mobile OFDM receiver ASIC," in *Proc. IEEE Wireless Commun. Netw. Conf.*, vol. 4, 2004, pp. 2120–2124.

[22] G. Leschhorn and R. Young, *Handbook of LED and SSL Metrology*. Berlin, Germany: Pro BUSINESS GmbH, 2017.

[23] M. Kavehrad, M. S. Chowdhury, and Z. Zhou, *Short-Range Optical Wireless: Theory and Applications*. Hoboken, NJ, USA: Wiley, 2016.

[24] J. M. Kahn and J. R. Barry, "Wireless infrared communications," *Proc. IEEE*, vol. 85, no. 2, pp. 265–298, Feb. 1997.

[25] S. Ghosh, H.-T. Wang, and W. D. Leon-Salas, "A circuit for energy harvesting using on-chip solar cells," *IEEE Trans. Power Electron.*, vol. 29, no. 9, pp. 4658–4671, Sep. 2014.

[26] R. M. Corless, G. H. Gonnet, D. E. G. Hare, D. J. Jeffrey, and D. E. Knuth, "On the Lambert W function," *Adv. Comput. Math.*, svol. 5, pp. 329–359, Dec. 1996.

[27] R. A. Kumar, M. S. Suresh, and J. Nagaraju, "Time domain technique to measure solar cell capacitance," *Rev. Sci. Instrum.*, vol. 74, no. 7, pp. 3516–3519, 2003.

[28] Texas Instruments. *INA322—Micropower, Single-Supply, CMOS Instrumentation Amplifier*. Accessed: Feb. 14, 2020. [Online]. Available: http://www.ti.com/lit/ds/symlink/ina322.pdf

[29] Texas Instruments. *TLVx379—Cost-Optimized, Low-Voltage, 4-µA, Rail-to-Rail I/O Operational Amplifiers*. Accessed: Feb. 14, 2020. [Online]. Available: http://www.ti.com/lit/ds/symlink/tlv379.pdf

[30] Texas Instruments. *TLV701x and TLV702x Small Size, Low-Power, Low-Voltage Comparators*. Accessed: Feb. 14, 2020. [Online]. Available: http://www.ti.com/lit/ds/symlink/tlv7022.pdf

[31] Texas Instruments. *TLV2401, TLV2402, TLV2404 Family of 880 nA/ch Rail-to-Rail Input/Output Operational Amplifiers With Reverse Battery Protection*. Accessed: Feb. 25, 2020. [Online]. Available: https://www.ti.com/lit/ds/symlink/tlv2401.pdf

[32] I. Y. W. Chung and C. Liang, "A low-cost photovoltaic energy harvesting circuit for portable devices," in *Proc. Int. Conf. Power Electron. Drive Syst.*, 2011, pp. 334–339.

[33] H. Kim, S. Kim, C.-K. Kwon, Y.-J. Min, C. Kim, and S.-W. Kim, "An energy-efficient fast maximum power point tracking circuit in an 800-µW photovoltaic energy harvester," *IEEE Trans. Power Electron.*, vol. 28, no. 6, pp. 2927–2935, Jun. 2012.

[34] X. Liu, L. Huang, K. Ravichandran, and E. Sanchez-Sinencio, "A highly efficient reconfigurable charge pump energy harvester with wide harvesting range and two-dimensional MPPT for Internet of Things," *IEEE J. Solid-State Circuits*, vol. 51, no. 5, pp. 1302–1312, May 2016.

[35] S. Stanzione, C. van Liempd, R. van Schaijk, Y. Naito, R. F. Yazicioglu, and C. van Hoof, "A self-biased 5-to-60V input voltage and 25-to-1600µW integrated DC–DC buck converter with fully analog MPPT algorithm reaching up to % end-to-end efficiency," in *Proc. IEEE Int. Solid-State Circuits Conf.*, 2013, pp. 74–75.

[36] Lumileds. *LUXEON Rebel Color Line*. Accessed: Apr. 13, 2020. [Online]. Available: https://www.lumileds.com/uploads/265/DS68-pdf

[37] D. Kwon and G. A. Rincon-Mora, "A single-inductor AC-DC piezoelectric energy-harvester/battery-charger IC converting ±(0.35 to 1.2 V) to (2.7 to 4.5 V)," in *Proc. IEEE Int. Solid-State Circuits Conf. ISSCC)*, 2010, pp. 494–495.

[38] *Forward Error Correction for High Bit-Rate DWDM Submarine Systems*, document ITU-T G.975.1, ITU, Geneva, Switzerland, 2004. Accessed: Apr. 17, 2020. [Online]. Available: https://www.itu.int/rec/TREC-G.975.1-200402-I/en

[39] J. Abu-Ghalune and M, Alja'Fari, "Parallel data transmission using new line code methodology," *Int. J. Netw. Commun.*, vol. 6, no. 5, pp. 98–101, 2016.

Walter D. Leon-Salas (Member, IEEE) received the B.S. degree in electronic engineering from the Universidad Nacional de San Agustin, Arequipa, Peru, and the M.S. and Ph.D. degrees in electrical engineering from the University of Nebraska-Lincoln in 2001 and 2006, respectively. He is an Associate Professor with the School of Engineering Technology, Purdue University. From 2007 to 2012, he was with the University of Missouri-Kansas City. His research interests include optical communications, imaging, data compression, and energy harvesting. In 2011, he received the CAREER Award from the National Science Foundation.

Xiaozhe Fan was born in Taiyuan, China, in 1990. He received the B.Sc. degree in electrical engineering from the Tianjin University of Science and Technology, in June 2013, and the Ph.D. degree in electrical engineering technology from Purdue University, in 2021. His research interests include optical frequency identification technology, energy harvesting, and self-powered wireless sensor applications.

Jongseok Kim received the B.Eng. degree in mechanical and automotive engineering and electrical and electronic engineering from the University of Ulsan, Ulsan, South Korea. He is currently pursuing the M.Sc. degree with CCS Graduate School of Green Transportation, Korea Advanced Institute of Science and Technology, Daejeon, South Korea. From 2019 to 2020, he was a Visiting Scholar with Integrated Circuits and Systems Lab, Purdue University, West Lafayette, IN, USA. His research interests include optical communication, energy harvesting, motor, and inverter control and inverter topologies.

Borja Peleato received the M.S. and Ph.D. degrees in electrical engineering from Stanford University, Stanford, CA, USA, in 2009 and 2013, respectively. From 2014 to 2020, he was an Assistant Professor with ECE Department, Purdue University, West Lafayette, IN, USA, and in 2020 he joined STC Group, Universidad Carlos III de Madrid, Spain. His research interests include wireless communications, signal processing for nonvolatile storage, and convex optimization.

Saeed Mohammadi received the Ph.D. degree in electrical engineering from the University of Michigan, Ann Arbor, in 2000. He is currently a Professor of Electrical and Computer Engineering with Purdue University, West Lafayette, IN, USA. He has published more than 200 conference and journal papers on these subjects. His research interests include CMOS ultra-low-power electronics, CMOS for mm-wave applications, flexible electronics, and Si-based vacuum electronics.

Sindhubala Kadirvelu received the B.E. degree from Anna University, Chennai, India, in 2009, and the M.Tech. degree from VIT University, Vellore, India, in 2011. She is currently pursuing the Ph.D. degree with the Department of Electronics and Communication Engineering, B. S. Abdur Rahman Crescent Institute of Science and Technology, Chennai, India. From 2011 to 2014, she worked as a Programmer Analyst with Cognizant Technology Solutions. From 2019 to 2020, she was a Visiting Scholar with Purdue University. Her research interests include optical wireless communications, visible light communication, and energy harvesting.

B. Vijayalakshmi received the master's degree from Anna University, Chennai. She is currently serving as a Professor with the Electronics and Communication Engineering Department, B. S. Abdur Rahman Crescent Institute of Science and Technology, Chennai. She has published more than 30 papers in various international and national journals and conferences. Her current research interests include image processing, noise removal, optical communication, perceptual image analysis, 3-D scene generation, antenna design, energy harvesting, and LiFi communication with solar cell.